

RINO: Accurate, Robust Radar-Inertial Odometry with Non-Iterative Estimation*

Shuocheng Yang, Yueming Cao, Shengbo Li, Jianqiang Wang and Shaobing Xu[✉]

Abstract—Precise localization and mapping are critical for achieving autonomous navigation in self-driving vehicles. However, ego-motion estimation still faces significant challenges, particularly when GNSS failures occur or under extreme weather conditions (e.g., fog, rain, and snow). In recent years, scanning radar has emerged as an effective solution due to its strong penetration capabilities. Nevertheless, scanning radar data inherently contains high levels of noise, necessitating hundreds to thousands of iterations of optimization to estimate a reliable transformation from the noisy data. Such iterative solving is time-consuming, unstable, and prone to failure. To address these challenges, we propose an accurate and robust Radar-Inertial Odometry system, RINO, which employs a non-iterative solving approach. Our method decouples rotation and translation estimation and applies an adaptive voting scheme for 2D rotation estimation, enhancing efficiency while ensuring consistent solving time. Additionally, the approach implements a loosely coupled system between the scanning radar and an inertial measurement unit (IMU), leveraging Error-State Kalman Filtering (ESKF). Notably, we successfully estimated the uncertainty of the pose estimation from the scanning radar, incorporating this into the filter’s Maximum A Posteriori estimation, a consideration that has been previously overlooked. Validation on publicly available datasets demonstrates that RINO outperforms state-of-the-art methods and baselines in both accuracy and robustness. Our code is available at <https://github.com/yangsc4063/rino>.

Note to Practitioners—The localization technology for autonomous vehicles faces significant challenges under adverse conditions such as fog, rain, and snow. Current sensors commonly mounted on vehicles, such as cameras and LiDAR, are ineffective in such weather, and traditional odometry methods based on these sensors are prone to failure. Scanning millimeter-wave radar, with its strong penetration capabilities, can provide dense, wide-ranging, and robust perception under such conditions, making it a promising alternative. However, radar data is often noisy and prone to ghosting artifacts, making processing challenging and hindering its widespread research and practical application. In this paper, we propose a Radar-Inertial Odometry (RINO) system that integrates pose estimation from scanning radar and IMU sensors along with uncertainty estimation within a non-iterative point cloud registration framework. Experimental validation on both datasets and real vehicles shows that RINO outperforms existing methods in terms of accuracy, efficiency, and robustness, providing a powerful solution for autonomous driving technologies in adverse weather conditions.

Index Terms—Scanning radar; SLAM; Pointcloud registration; State estimation

* This work was supported by the National Natural Science Foundation of China (No. 52372415, 52221005).

The authors are with the School of Vehicle and Mobility, Tsinghua University, Beijing 100084, China yangsc4063@gmail.com, shaobxu@tsinghua.edu.cn

✉ Corresponding author.

I. INTRODUCTION

Autonomous vehicles rely on precise localization to ensure safe and efficient navigation. The Global Navigation Satellite System (GNSS) is commonly employed and highly effective; however, its performance can degrade in urban environments due to obstructions such as trees and tall buildings. Consequently, there is increasing interest in leveraging onboard sensors for ego-motion estimation, either to augment or fully substitute GNSS-based systems, particularly during GNSS outages.

Over the past two decades, numerous odometry and SLAM methods have been developed based on camera [1]–[6] and LiDAR [7]–[11] all of which have demonstrated excellent performance. However, these methods are often limited by adverse weather conditions, such as fog, rain, or snow. In contrast, millimeter-wave radar, due to its longer operating wavelengths, can perform robustly under such conditions, emerging as a promising alternative. Unfortunately, scanning radar data is inherently noisy and prone to significant distortion, which presents challenges for the design of effective odometry or SLAM methods.

Given these challenges, an increasing number of researchers are exploring solutions in radar-based odometry [12]. Existing methods for radar odometry based on scanning radar can be broadly categorized into sparse and dense techniques. Dense methods directly process the tensor-format data acquired by scanning radar, whereas sparse methods extract key points from this data before performing registration. In terms of computational complexity and accuracy, sparse methods tend to offer advantages. Most sparse methods are derived from local point cloud registration using the Iterative Closest Point (ICP) algorithm [13], an iterative approach that alternates between nearest point matching and registration residuals to align two scans of point clouds. Although iterative methods can effectively mitigate the influence of outliers over successive iterations and approximate the optimal estimation, they also have inherent drawbacks: high computational cost, instability, and susceptibility to local minima, which may lead to failure.

To address the aforementioned challenges, we propose a radar-inertial odometry (RIO) system, **RINO**, that eliminates the need for iterative solving of rotation and translation between two scans. Building upon the ORORA framework [14] as a baseline, RINO adopts its workflow for the scanning radar odometry (RO) branch while retaining its method for modeling the anisotropic uncertainty of keypoints extracted from raw radar data. In contrast to ORORA, the scanning radar branch of RINO improves keypoint extraction, imple-

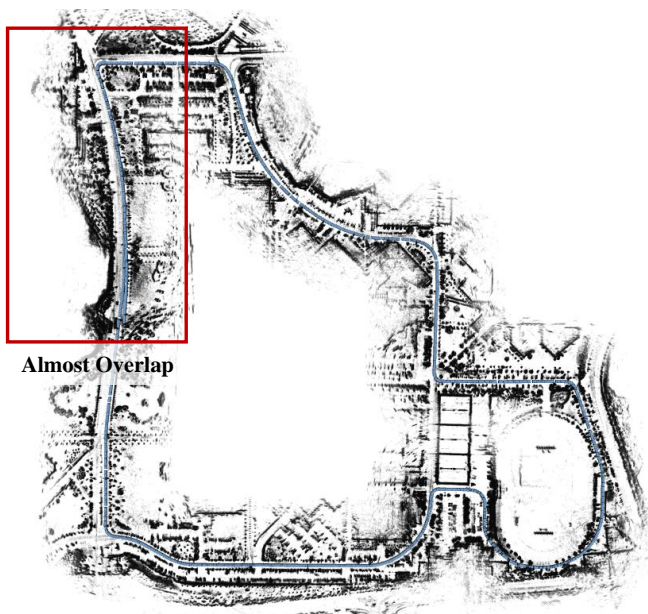


Fig. 1. Trajectories obtained by the proposed radar-inertial odometry (RIO) system using the KAIST02 sequence of the Mulran dataset. The raw radar data and IMU data of the KAIST02 sequence are given in the format of ROS messages using the File player provided by the Mulran dataset and can run robustly in real time after being processed by RINO. The trajectory of the second lap almost overlaps with that of the first lap, demonstrating the accuracy of RINO.

ments motion distortion compensation, and avoids iterative solving by employing an adaptive voting technique for rotation and translation estimation. Moreover, we were unexpectedly able to leverage the adaptive voting method to quantify the uncertainty of pose estimation. Consequently, we introduce an inertial measurement unit (IMU), resulting in a loosely coupled odometry system based on error-state Kalman filtering (ESKF), which successfully integrates the pose estimation uncertainty from the radar branch into the filter's Maximum A Posteriori estimation. For the first time, we incorporate the current state estimation quality of each sensor into the loosely coupled system, rather than modularly fusing their outputs. Given that the IMU is also adaptable to adverse weather conditions, we believe the entire system is capable of handling such challenges as well. The main contributions of this paper are as follows:

- A non-iterative method for rotation and translation estimation suitable for high-noise and significantly distorted scanning radar data. This approach not only reduces computation time but also enhances the robustness of the estimation process.
- A loosely coupled ESKF system, where RINO enables the online computation of pose estimation uncertainty from the scanning radar, which is adaptively fused with the IMU. This enhances the environmental adaptability of the system.
- Extensive experiments on datasets demonstrate that RINO exhibits strong performance and adaptability across various scenarios and adverse weather conditions. Real-vehicle testing further validates the practicality of RINO.

II. RELATED WORKS

A. Radar Odometry

In the past decade, development of odometry systems based on scanning radar attracted the attention of several research teams around the world. Scanning radar data is intriguing as it can be represented both as dense data similar to images and as sparse data by extracted keypoints akin to pointcloud. Consequently, we roughly classify these research methods into two categories: dense methods and sparse methods.

Dense methods directly process raw or minimally pre-processed tensor-format data from scanning radar, originating from the direct method in visual odometry. Inspired by Fourier-Mellin Transformation (FMT), methods such as [15]–[17] have been developed. However, these methods require substantial computational resources and struggle with dynamic distortion and Doppler shift compensation.

Sparse methods generally involve two steps: firstly, extracting keypoints from raw images of scanning radar, and subsequently solving the pointcloud registration problem.

One typical sparse method originates from LiDAR odometry (LO), requiring iterative solving transformation and rotation between consecutive scans. [18]–[22] have applied the classic LO algorithms, such as point-to-line ICP or NDT, to scanning radar with satisfactory results. However, these iterative methods heavily rely on initial values and online optimizations, making them less robust.

The other type of sparse method stems from the indirect methods in visual odometry, typically utilizing feature descriptors to describe and match keypoints from two scans. However, descriptor-based matching inevitably introduces errors, leading to a high proportion of outliers among the keypoints. The presence of high noise and "ghosting" artifacts in scanning radar exacerbates this issue. Therefore, the primary challenge of these methods is how to effectively identify and remove outliers. Hong et al. [23], [24] used distance consistency between pairwise points as a constraint to remove outliers and then used SVD decomposition to analytically solve for rotation. Barnes et al. [25] employed a U-net [26] style CNN to simultaneously extract keypoints and generate per-point descriptors. While the keypoints matching after training is relatively accurate, its generalization performance is poor. Burnett et al. [27] utilized the classic RANSAC method to remove outliers in keypoint matching and demonstrated the necessity of incorporating dynamic distortion compensation into scanning radar-based odometry.

Recently, researchers have recognized a major advantage of these methods: good transferability to pointcloud registration techniques active in the CV field. These techniques offer novel solutions for pointcloud registration with outliers or low overlap. TEASER [28] models the robust pointcloud registration problem using truncated least squares, decoupling the estimation of scaling, rotation, and translation. It applies Max Clique Inlier Selection (MCIS), Graduated Nonconvexity (GNC), and adaptive voting in a cascaded manner, significantly improving the accuracy, efficiency, and robustness of the solution. SC2-PCR (Second-Order Spatial Compatibility Point Cloud Registration) [29] describes the spatial compatibility

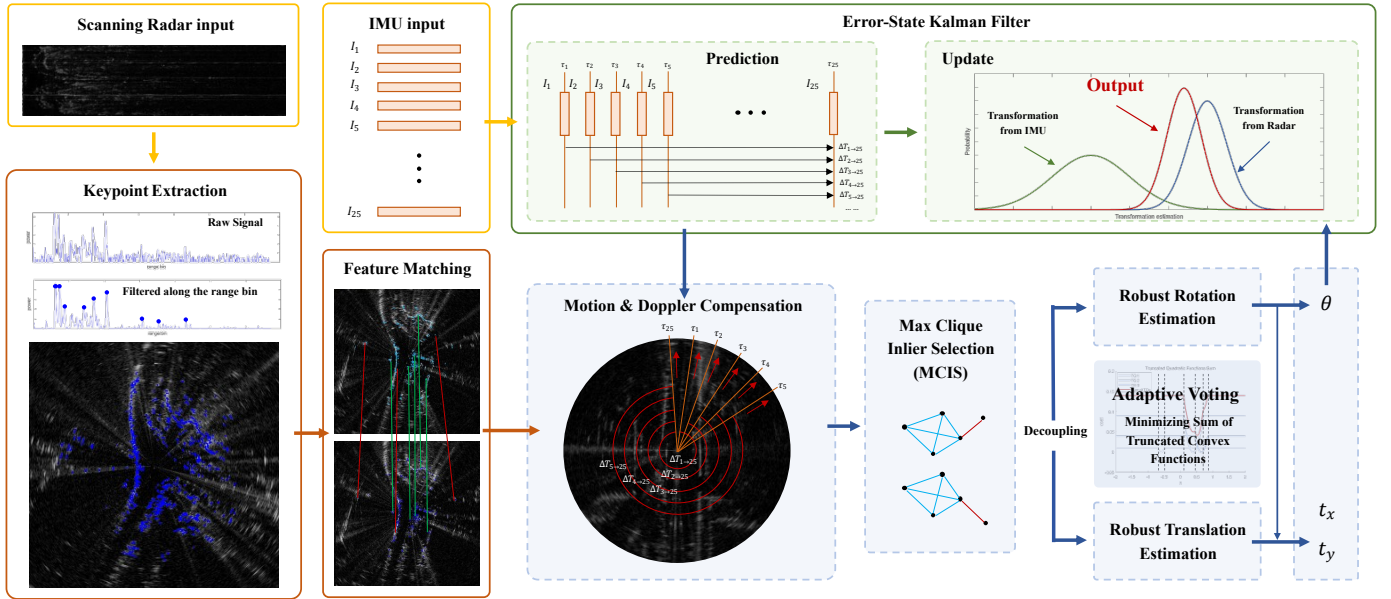


Fig. 2. The workflow of RINO consists of two branches. The IMU branch is responsible for constructing the motion equations and performing motion distortion compensation. The Radar branch extracts and matches keypoints from raw radar data. After selecting inliers based on the maximum clique, it non-iteratively estimates the rotation and translation between two scans, along with their uncertainties. The output of the Radar branch is then fused with the IMU's predictions as observations, leading to the optimal pose estimation.

between consecutive pointclouds using a graph and proposes a spectral matching technique based on a second-order spatial compatibility matrix. MAC [30], building upon SC2-PCR, relaxes maximum clique constraints to maximal cliques, allowing the pointcloud registration to consider global consistency as much as possible rather than just local consistency. A recent work, ORORA [14], drew inspiration from TEASER and specifically modeled the anisotropic uncertainty of keypoints extracted from Navtech scanning radar. Extensive experiments demonstrate that ORORA not only achieves state-of-the-art performance in odometry accuracy among similar methods but also exhibits more robust real-time self-motion estimation performance, indicating it as a research direction worthy of further exploration. However, for scanning radar data with high noise, our validation suggests that the latter two methods are not suitable, mainly because they do not model and analyze the uncertainty of the pointcloud positions themselves.

We select the ORORA as a baseline pipeline and design module to consider the uncertainty, as well as further improve the pipeline to better handle scanning radar. For example, (1) the GNC method used in its rotation estimation branch is designed for 3D rotation estimation and appears somewhat redundant when used with scanning radar, a 2D sensor. (2) The GNC method requires multiple iterations, which results in unstable computation time and somewhat relies on initial values, incurring possible estimation failure. This paper takes ORORA as the baseline and employs adaptive voting to achieve uniformity in transformation estimation (i.e., rotation and translation), thereby addressing the aforementioned issues.

B. Radar-Inertial Odometry

In addition to utilizing individual sensors, several studies [31] [32] have focused on ego-motion estimation by fusing

traditional radar and IMU data using Kalman filtering (KF) and its various derivatives. Kalman filtering-based fusion can be broadly categorized into loosely coupled and tightly coupled methods. Tightly coupled methods integrate the scanning radar point cloud registration residuals into the observations; however, these approaches rely on the equivalence between the Invariant Extended Kalman Filter (IEKF) and the Gauss-Newton method, which conflicts with the non-iterative estimation employed in the RINO scanning radar branch.

Fortunately, we discovered that the adaptive voting method allows for the simultaneous estimation of both pose and its uncertainty. By feeding both the pose and uncertainty into the Maximum A Posteriori (MAP) estimation module of the loosely coupled system, we effectively enhance the determinism of the previously modular fusion. RINO is capable of estimating the confidence of pose estimates from both sensors based on current sensor data and adaptively fusing these estimates, thereby improving the system's stability. Notably, to the best of our knowledge, no existing work has fused scanning radar with IMU data in this manner.

III. METHODOLOGY

A. System Overview

The proposed workflow called **RINO** is shown in Fig. 2. It receives scanning radar (4Hz) and IMU data (100Hz) simultaneously. We aim to use observation of these two sensors to estimate the state of the vehicle. General state estimation can be formulated as a Maximum A Posteriori (MAP) problem. Assuming the motion process exhibits Markovian properties, this problem can be solved by filtering methods, which is advantageous due to its lightweight nature. In the filter, IMU measurements are used to construct the prediction equation as the prior estimate of the motion state, while the registration

results from scanning radar branch serve as the observation for the pose. In the following, the two branches of RINO are introduced respectively.

B. State Estimations

For the IMU, its state variables consist of:

$$\mathbf{x} = [\mathbf{p}, \mathbf{v}, \mathbf{R}, \mathbf{b}_g, \mathbf{b}_a, \mathbf{g}]^\top \quad (1)$$

where \mathbf{p} and $\mathbf{R} \in \text{SO}(3)$ are the position and altitude of IMU, \mathbf{v} is the velocity, $\mathbf{b}_g, \mathbf{b}_a$ is the IMU bias and \mathbf{g} is gravity. These variables are relative to the world coordinate system. However, when constructing the motion equations with these state variables, linearizing the rotation variables becomes a challenging problem. Inspired by the Fast-lio [8], we treat the original state variables as nominal state variables, where the difference between the nominal and true values represents the error state variables. Moreover, the handling of noise is incorporated into the error state variables. The kinematic equations for nominal state variables are

$$\begin{aligned} \mathbf{p}(t + \Delta t) &= \mathbf{p} + \mathbf{v}\Delta t + \frac{1}{2}(\mathbf{R}(\mathbf{a}_I - \mathbf{b}_a))\Delta t^2 + \frac{1}{2}\mathbf{g}\Delta t^2, \\ \mathbf{v}(t + \Delta t) &= \mathbf{v} + \mathbf{R}(\mathbf{a}_I - \mathbf{b}_a)\Delta t + \mathbf{g}\Delta t, \\ \mathbf{R}(t + \Delta t) &= \mathbf{R} \cdot \text{Exp}((\boldsymbol{\omega}_I - \mathbf{b}_g)\Delta t), \\ \mathbf{b}_g(t + \Delta t) &= \mathbf{b}_g, \mathbf{b}_a(t + \Delta t) = \mathbf{b}_a, \mathbf{g}(t + \Delta t) = \mathbf{g}. \end{aligned} \quad (2)$$

And error state variables in discrete time are

$$\begin{aligned} \delta \mathbf{p}(t + \Delta t) &= \delta \mathbf{p} + \delta \mathbf{v}\Delta t, \\ \delta \mathbf{v}(t + \Delta t) &= \delta \mathbf{v} + (-\mathbf{R}(\mathbf{a}_I - \mathbf{b}_a)^\wedge \delta \boldsymbol{\theta} - \mathbf{R}\delta \mathbf{b}_a + \delta \mathbf{g})\Delta t - \boldsymbol{\eta}_v, \\ \delta \boldsymbol{\theta}(t + \Delta t) &= \text{Exp}(-(\boldsymbol{\omega}_I - \mathbf{b}_g)\Delta t)\delta \boldsymbol{\theta} - \delta \mathbf{b}_g\Delta t - \boldsymbol{\eta}_\theta, \\ \delta \mathbf{b}_g(t + \Delta t) &= \delta \mathbf{b}_g + \boldsymbol{\eta}_g, \delta \mathbf{b}_a(t + \Delta t) = \delta \mathbf{b}_a + \boldsymbol{\eta}_a, \\ \delta \mathbf{g}(t + \Delta t) &= \delta \mathbf{g}. \end{aligned} \quad (3)$$

where Δt denotes the discrete time step. \mathbf{a}_I and $\boldsymbol{\omega}_I$ are the measurements of IMU, while $\boldsymbol{\eta}_a$ and $\boldsymbol{\eta}_g$ are white noise of IMU measurements. $\boldsymbol{\eta}_v$ is the result of $\boldsymbol{\eta}_a$ acting on velocity, satisfying $\sigma(\boldsymbol{\eta}_v) = \Delta \sigma(\boldsymbol{\eta}_a)$, and likewise for $\boldsymbol{\eta}_\theta$.

Based on Eq.(2) and (3), we perform the prediction process of the ESKF. Since the noise has been incorporated into the error states, the prediction of nominal state variables can be directly obtained from equation Eq.(2). As for the error states,

$$\begin{aligned} \delta \mathbf{x}_{\text{pred}} &= \mathbf{A}\delta \mathbf{x} + \boldsymbol{\eta}, \\ \mathbf{P}_{\text{pred}} &= \mathbf{A}\mathbf{P}\mathbf{A}^\top + \mathbf{B}. \end{aligned} \quad (4)$$

where \mathbf{P} is the estimate covariance matrix of error state variables $\delta \mathbf{x}$, \mathbf{A} is the coefficient matrix obtained from expressing (3) in matrix multiplication form, and \mathbf{B} is the noise matrix of $\delta \mathbf{x}$, where the covariance matrices of individual variables' noises are arranged diagonally.

Following the prediction step of the ESKF, the pose is computed at a high frequency of 100Hz, consistent with the IMU output frequency. These high-frequency yet coarse pose estimates can partially alleviate the dynamic distortions in single-frame data from the scanning radar. The specific methodology will be elaborated in Sec.III-C.

In the update process of ESKF, the position and attitude output from RO can be considered as observations for the state variables in the RIO system. Let $\mathbf{p}_{\text{radar}}$ and $\mathbf{R}_{\text{radar}}$ represent the observations from RO at a certain moment. We can directly express them as observations to the error state variables.

$$\delta \mathbf{z} = [\mathbf{p}_{\text{radar}} - \mathbf{p}, \text{Log}(\mathbf{R}^\top \mathbf{R}_{\text{radar}})]^\top \quad (5)$$

Consequently, the observation equation becomes remarkably simple:

$$\begin{aligned} \mathbf{p}_{\text{radar}} - \mathbf{p} &= \delta \mathbf{p} + \boldsymbol{\xi}_p, \\ \text{Log}(\mathbf{R}^\top \mathbf{R}_{\text{radar}}) &= \delta \boldsymbol{\theta} + \boldsymbol{\xi}_\theta \end{aligned} \quad (6)$$

where $\boldsymbol{\xi}_p$ and $\boldsymbol{\xi}_\theta$ are noise of observations from RO (In other words, the uncertainty of the scanning radar pose estimation). Similarly, write Eq.(6) in its overall form:

$$\delta \mathbf{z} = \mathbf{C}\delta \mathbf{x} + \boldsymbol{\xi}, \quad (7)$$

the observation matrix \mathbf{C} can be easily provided as:

$$\mathbf{C} = \begin{bmatrix} \mathbf{I}_3 & \mathbf{0} & \mathbf{0} & \mathbf{0} & \mathbf{0} & \mathbf{0} \\ \mathbf{0} & \mathbf{0} & \mathbf{I}_3 & \mathbf{0} & \mathbf{0} & \mathbf{0} \end{bmatrix}, \quad (8)$$

the noise matrix is $\mathbf{D} = \text{diag}(\text{Cov}(\boldsymbol{\xi}_p), \text{Cov}(\boldsymbol{\xi}_\theta))$. With these steps, the update process of ESKF can be executed as follows:

$$\begin{aligned} \mathbf{K} &= \mathbf{P}_{\text{pred}}\mathbf{H}^\top(\mathbf{C}\mathbf{P}_{\text{pred}}\mathbf{C}^\top + \mathbf{D})^{-1}, \\ \delta \hat{\mathbf{x}} &= \delta \mathbf{x}_{\text{pred}} + \mathbf{K}(\delta \mathbf{z} - \mathbf{C}\delta \mathbf{x}_{\text{pred}}), \\ \mathbf{P} &= (\mathbf{I} - \mathbf{K}\mathbf{C})\mathbf{P}_{\text{pred}}. \end{aligned} \quad (9)$$

where $c(\cdot)$ represents the observation function.

After prediction and update steps, it's necessary to incorporate the error states into the nominal states, i.e., to reset the ESKF (setting $\delta \mathbf{x} = 0$). It's important to note that resetting the error state variables will result in a change in the zero point of the rotation variable's tangent space. Therefore, the covariance matrix should be adjusted accordingly

$$\begin{aligned} \mathbf{J} &= \text{diag}(\mathbf{I}_3, \mathbf{I}_3, \mathbf{I}_3 - \frac{1}{2}\delta \boldsymbol{\theta}^\wedge, \mathbf{I}_3, \mathbf{I}_3, \mathbf{I}_3), \\ \mathbf{P}_{\text{reset}} &= \mathbf{J}\mathbf{P}\mathbf{J}^\top \end{aligned} \quad (10)$$

where $\delta \boldsymbol{\theta}$ represents the estimated error state variables before resetting, and $(\cdot)^\wedge$ denotes expressing the vector as a skew-symmetric matrix.

C. Scanning Radar Odometry

RO of the system follows a similar workflow to ORORA [14] which serves as the baseline. Firstly, keypoints are extracted from the raw intensity-distance-angle data of the scanning radar. Then, ORB [33] are used to generate descriptors for each point, followed by brute-force matching to establish correspondences set $\{(\mathbf{p}_i, \mathbf{q}_i)\}_{i=1}^N$ between keypoints from the previous scan $\{\mathbf{p}_i\}_{i=1}^N$ and current scan $\{\mathbf{q}_i\}_{i=1}^N$. Subsequently, compensation is applied to these correspondences for dynamic distortions and Doppler frequency shifts. Finally, the compensated point correspondences are used for pointcloud registration. The transformations from scan to scan are accumulated. We decouple the estimation of rotation and translation and employ an accelerated adaptive voting method, which enables fast computation of rotation and translation

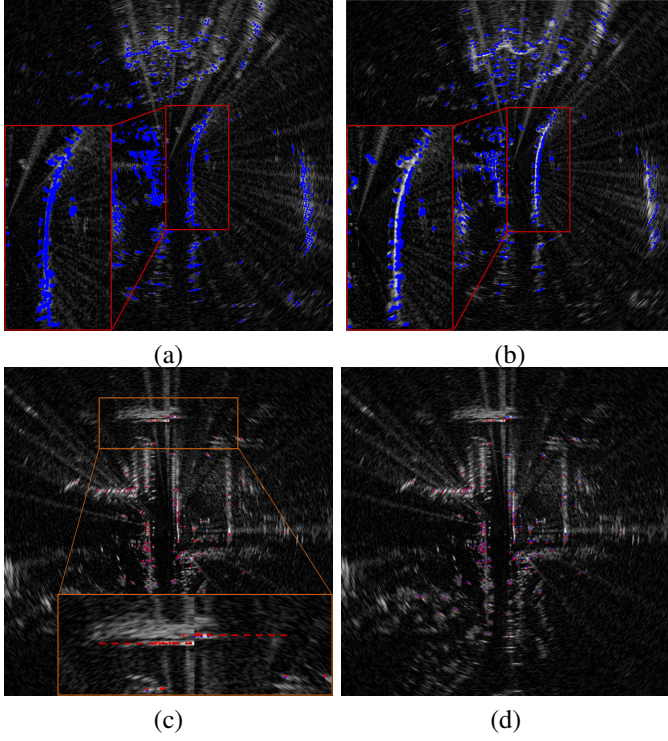


Fig. 3. (a) and (b) represent the keypoints extracted by the enhanced cen2018 and cen2019; (c) and (d) are the pointcloud before and after dynamic distortion compensation, where after compensation, the wall that was previously divided into two segments is restored to a straight line.

without the need for iteration. In the following, we focus on explaining the parts that differ from the baseline, while the remaining sections can be found in [14].

The quality of keypoints extracted from radar directly determines the clarity of the resulting pointcloud map. Upon evaluating cen2018 [34] and cen2019 [35], we found that the keypoint positions obtained from cen2018 were significantly more accurate. Consequently, cen2018 was selected for our application, and we impose a limit on the maximum distance for it, because points too far away exhibit high uncertainty, negatively affecting pointcloud registration. Moreover, a high-pass filtering to the raw data was applied to augment the distinctiveness of signal peaks, thereby refining the keypoint extraction process.

As mentioned earlier, we use high-frequency pose estimates from the IMU to compensate for dynamic distortions and Doppler frequency shifts. Let t_s denote the time for a single scan of the scanning radar. During $0 \sim t_s$, 25 pose estimates $\mathbf{T}_1, \mathbf{T}_2, \dots, \mathbf{T}_{\text{end}}$ from the IMU are received, each timestamped as $\tau_1, \tau_2, \dots, \tau_{\text{end}}$. By interpolating $\mathbf{T}_1, \mathbf{T}_2, \dots, \mathbf{T}_{\text{end}}$, we can query the radar pose at any time within $0 \sim t_s$. Therefore, we can transform the coordinates of any keypoint to τ_{end} to achieve motion compensation.

$$\mathbf{p}' = \mathbf{T}_{IR}^{-1} \mathbf{T}_{\text{end}}^{-1} \mathbf{T}_{\tau} \mathbf{T}_{IR} \mathbf{p}_{\tau} \quad (11)$$

Here, \mathbf{p}_{τ} is the coordinates of the keypoint at τ , \mathbf{T}_{τ} the interpolated IMU pose at τ , and \mathbf{T}_{IR} represents the extrinsic parameters between the IMU and the radar.

D. Pointcloud Registration With Non-iterative Solving

In Sec. III-C, it is mentioned that the correspondences within $\{(\mathbf{p}_i, \mathbf{q}_i)\}_{i=1}^N$ are used to perform pointcloud registration to achieve scan-to-scan odometry. We focus on explaining this part in detail below.

We describe the robust registration problem for scanning radar as follows:

$$\mathbf{q}_i = \mathbf{R}^{\circ} \mathbf{p}_i + \mathbf{t}^{\circ} + \mathbf{o}_i + \boldsymbol{\varepsilon}_i \quad (12)$$

where \mathbf{R}° and \mathbf{t}° respectively denote the true values of rotation and translation. \mathbf{o}_i indicates whether the correspondence for the i -th point is correct; if correct, $\mathbf{o}_i = 0$, otherwise \mathbf{o}_i can take any value. $\boldsymbol{\varepsilon}_i$ models the measurement noise.

Due to the presence of excessive noise and "ghosting" in the raw data from the scanning radar, the correspondence set $\{(\mathbf{p}_i, \mathbf{q}_i)\}_{i=1}^N$ contains a multitude of erroneous matches, as illustrated in the schematic diagram found in [14]. Therefore, we adopt truncated least squares (TLS) estimation to establish an optimization model for robust pointcloud registration, aiming to reduce sensitivity to outliers in the results as much as possible.

$$\min_{\mathbf{R} \in \text{SO}(2), \mathbf{t} \in \mathbb{R}^2} \sum_{i=1}^N \min \left\{ \frac{1}{\beta_i^2} \|\mathbf{q}_i - \mathbf{R} \mathbf{p}_i - \mathbf{t}\|^2, \bar{c}^2 \right\}, \quad (13)$$

It is worth noting that β_i in the Eq.(13) represents the primary variance of the noise $\boldsymbol{\varepsilon}_i$ (the upper bound of the variance after projecting the two-dimensional Gaussian distribution onto each direction). This implies that the model may appear rather coarse when describing keypoints from scanning radar with significant anisotropic uncertainty.

To better capture the uncertainty of keypoints and reduce problem complexity, we decouple the rotation and translation. In detail, we subtract pairs of points within the same scan of pointcloud to eliminate the translation transformation, resulting in translation-invariant measurements (TIMs).

$$\begin{aligned} \mathbf{q}_j - \mathbf{q}_i &= \mathbf{R}^{\circ} (\mathbf{p}_j - \mathbf{p}_i) + (\mathbf{o}_j - \mathbf{o}_i) + (\boldsymbol{\varepsilon}_j - \boldsymbol{\varepsilon}_i), \\ \mathbf{q}_{ij} &= \mathbf{R}^{\circ} \mathbf{p}_{ij} + \mathbf{o}_{ij} + \boldsymbol{\varepsilon}_{ij}, \quad i, j = 1, \dots, N, i \neq j \end{aligned} \quad (14)$$

Then, we calculate the magnitude of the translation-invariant measurements to obtain translation-rotation invariant measurements (TRIMs).

$$\begin{aligned} \|\mathbf{q}_{ij}\| &= \|\mathbf{R}^{\circ} \mathbf{p}_{ij} + \mathbf{o}_{ij} + \boldsymbol{\varepsilon}_{ij}\|, \\ \|\mathbf{q}_{ij}\| &= \|\mathbf{p}_{ij}\| + \tilde{o}_{ij} + \tilde{\varepsilon}_{ij}, \quad i, j = 1, \dots, N, i \neq j \end{aligned} \quad (15)$$

where $\tilde{o}_{ij} \leq \|\mathbf{o}_{ij}\|$, and $\tilde{\varepsilon}_{ij} \leq \|\boldsymbol{\varepsilon}_{ij}\|$.

We first use TRIMs $\{(\|\mathbf{p}_k\|, \|\mathbf{q}_k\|)\}_{k=1}^{N(N-1)/2}$ for preliminary inlier selection, where we only need to check if $|\|\mathbf{q}_k\| - \|\mathbf{p}_k\||$ is less than a predefined threshold. Like [14] [23], we also employ maximum clique search to address this issue. For detailed descriptions, please refer to their works.

Next, we can use TIMs $\{(\mathbf{p}_k, \mathbf{q}_k)\}_{k=1}^K$, $K \leq \frac{N(N-1)}{2}$ to estimate the rotation transformation, and then use $\hat{\mathbf{R}}$ to estimate the two components of the translation transformation separately.

$$\hat{\mathbf{R}} = \arg \min_{\mathbf{R} \in \text{SO}(2)} \sum_{k=1}^K \min \left\{ \frac{1}{\sigma_{R,k}^2} \|\mathbf{q}_k - \mathbf{p}_k\|^2, \bar{c}^2 \right\}, \quad (16)$$

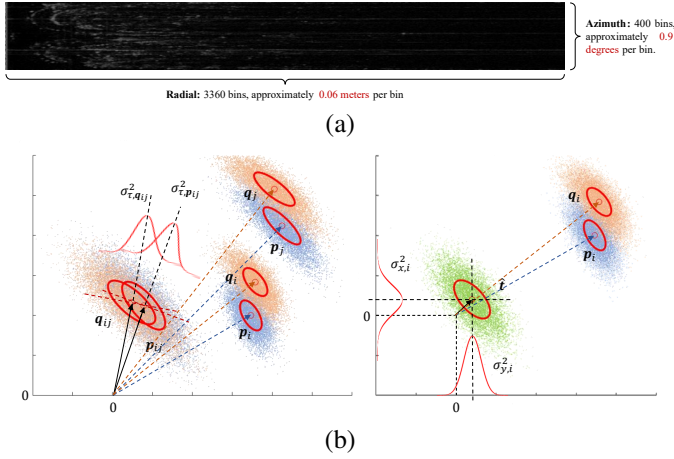


Fig. 4. (a) The raw data of scanning radar clearly exhibits significantly higher resolution in the radial direction compared to the angular direction. This results in severe anisotropic uncertainty in the keypoints extracted from it. (b) The variances of the rotation estimates (left) and translation estimates (right) are calculated from the uncertainty model of the keypoints.

$$\hat{t}_j = \arg \min_{t_j \in \mathbb{R}} \sum_{i=1}^N \min \left\{ \frac{1}{\sigma_{j,i}^2} (t_j - [q_i - \hat{R}p_i]_j)^2, \bar{c}^2 \right\}, j = 1, 2 \quad (17)$$

ORORA adopts the Graduated Non-Convexity (GNC) approach for rotation estimation, an efficient technique in addressing non-convex optimization challenges. However, GNC's iterative nature can result in unstable computation times and a potential to converge to local minima, which may introduce discontinuities in trajectory estimation. To overcome these limitations, we unify the optimization problems for rotation and translation estimation and implement a non-iterative solution using an adaptive voting method. Furthermore, we obtained the variances of the rotation and translation estimates to serve as inputs for the update process of ESKF.

It can be observed that a two-dimensional rotation can be expressed as a scalar (rotation angle). Therefore, (14) and (16) can be rewritten as:

$$\text{Ang}(\mathbf{q}_k) = \text{Ang}(\mathbf{p}_k) + \theta^\circ + \text{Ang}(\mathbf{o}_k) + \text{Ang}(\boldsymbol{\varepsilon}_k), \quad (18)$$

$$\hat{\theta} = \arg \min_{\theta \in \mathbb{R}} \sum_{k=1}^K \min \left\{ \frac{1}{\sigma_{\theta,k}^2} [\theta - (\text{Ang}(\mathbf{q}_k) - \text{Ang}(\mathbf{p}_k))]^2, \bar{c}^2 \right\} \quad (19)$$

Where $\text{Ang}(\cdot)$ represents the function to compute the argument (angle) of a vector.

It reveals that the objective functions in (19) and (17) actually have the same form: the sum of truncated quadratic functions with scalar variables. For such optimization problems, two key issues need to be considered. Firstly, how to estimate the variance of decision variables. Secondly, how to solve the problem itself.

Considering the first issue, the variances of rotation and translation originate from the uncertainty of keypoints.

$$\theta_k = \text{Ang}(\mathbf{q}_k) - \text{Ang}(\mathbf{p}_k), k = 1, \dots, K, \quad (20)$$

$$\mathbf{t}_i = \mathbf{q}_i - \hat{R}\mathbf{p}_i, i = 1, \dots, N, \quad (21)$$

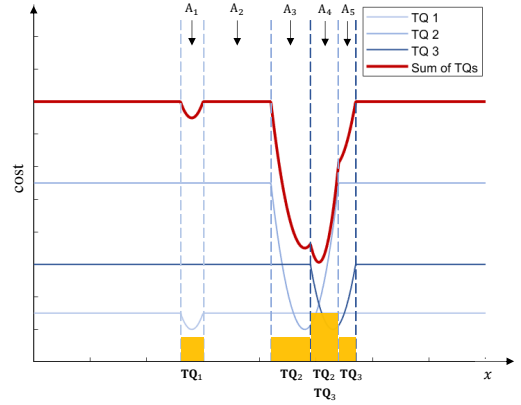


Fig. 5. The sum of three truncated quadratic functions. The truncation points of the same function are denoted by vertical lines of the same color. The entire domain is partitioned into a disjoint union of seven sets, among which five are non-trivial (A_1, \dots, A_5). Enumerating the local minima of the convex functions over A_1, \dots, A_5 , it can be inferred that the local minimum on A_4 is the global optimal solution.

Therefore, our discussion should start with modeling the uncertainty of keypoints. We highly appreciate ORORA's modeling of the anisotropic uncertainty of keypoints, so it is adopted. We assume that the uncertainty of keypoint $p_i(\rho_i, \phi_i)$ follows independent normal distributions in the range and azimuth $\rho_i \sim \mathcal{N}(\rho_i^\circ, \sigma_\rho^2)$, $\phi_i \sim \mathcal{N}(\phi_i^\circ, \sigma_\phi^2)$, where σ_ρ^2 and σ_ϕ^2 can be estimated from the raw polar coordinate data of the scanning radar (Fig.4(a)). Following the derivation in [14], keypoint p_i is modeled as a normal distribution $p_i \sim \mathcal{N}(p_i, C_{p_i})$, where the value of C_{p_i} can also be found in [14].

For rotation, the covariance of TIMs' distribution can be computed from $C_{p_{ij}} = C_{p_i} + C_{p_j}$, and then projected onto the tangential direction, as shown in the left plot of Fig.4(b).

$$C'_{p_{ij}} = \mathbf{W}C_{p_{ij}}\mathbf{W}^\top \quad (22)$$

Here, \mathbf{W} is the matrix that transforms the covariance from the original coordinate to the one with p_{ij} as the axis. Then, we take the element (1,1) of C'_{ij} , denoted as $\sigma_{\tau, p_{ij}}^2$, and divide it by the magnitude of p_{ij} to approximate the variance of the distribution of $\text{Ang}(p_{ij})$. Then, according to (20), the variance of the rotation can be found:

$$\sigma_{\theta,k}^2 = \frac{\sigma_{\tau, p_{ij}}^2}{\|p_{ij}\|^2} + \frac{\sigma_{\tau, q_{ij}}^2}{\|q_{ij}\|^2} \quad (23)$$

For translation, we need to utilize the previously obtained rotation \hat{R} . From (21), the covariance of t_i can be expressed as $C_{t_i} = C_{q_i} + \hat{R}C_{p_i}\hat{R}^\top$. Next, as shown in the right plot of 4(b), we project the distribution of translation onto the x and y directions. In other words, we take the (1,1) and (2,2) elements of C_{t_i} , which respectively correspond to the variance of the first and second components of translation.

At last, we solve the optimization where the objective function is the sum of truncated quadratic functions. This is

the key to solving the pointcloud registration with non-iterative method. Express equations (19) and (17) in a unified form:

$$\hat{x} = \arg \min_{x \in \mathbb{R}} \sum_{m=1}^M \min \left\{ \frac{1}{\sigma_{x,m}^2} (x - x_m)^2, \bar{c}^2 \right\}, m = 1, \dots, M \quad (24)$$

From Fig.5, we observe that although the objective function is globally highly non-convex, it is effectively piecewise convex. By partitioning the domain according to truncation points $\{x_m - \sigma_{x,m}^2 \bar{c}^2, x_m + \sigma_{x,m}^2 \bar{c}^2\}_{m=1}^M$, the objective function can be constrained to be convex (even quadratic) on each segment. Enumerating all segments, minimizing the objective function on each segment, and selecting the minimum value among all local minima enable the determination of the global minimum.

Let $(x - x_m)^2 / \sigma_{x,m}^2$ be denoted as $f_m(x)$, and let the aforementioned segment be denoted as $\{A_n\}_{n=1}^{2M-1}$. Our objective is to compute the index set $I_n = \{m : f_m(x) \leq \bar{c}^2\}$ corresponding to each A_n . We have

$$\min_{x \in \mathbb{R}} \sum_{m=1}^M \min \left\{ f_m(x), \bar{c}^2 \right\} = \min_n \min_{x \in \mathbb{R}} \sum_{r \in I_n} f_r(x) \quad (25)$$

By enumerating to obtain the optimal segments as \hat{n} , the optimal estimator \hat{x} we seek is

$$\hat{x} = \left(\sum_{r \in I_{\hat{n}}} \frac{1}{\sigma_{x,r}^2} \right)^{-1} \sum_{r \in I_{\hat{n}}} \frac{x_r}{\sigma_{x,r}^2} \quad (26)$$

E. Pose uncertainty estimation

We found that RINO may encounter some extreme situations during operation. For example, the extracted feature points might be too sparse, or there might be too many dynamic objects between two frames, resulting in a small number of inlier points remaining after MCIS, as shown in . These issues could lead to a decrease in the confidence of the current scanning radar branch pose estimation. In such cases, we hope that RINO will be more inclined to trust the pose estimation from the IMU.

Naturally, we can estimate the variance of \hat{x} from (26).

$$\sigma_{\hat{x}}^2 = \left(\sum_{r \in I_{\hat{n}}} \frac{1}{\sigma_{x,r}^2} \right)^{-1} \quad (27)$$

In summary, the aforementioned adaptive voting is used to estimate rotation angle and the two components of translation separately, along with their uncertainty. Subsequently, these three estimators and their uncertainty can be input as observation into the update process of the Kalman filter in Sec.III-B, thereby completing the adaptive, loosely coupled state estimation between the scanning radar and the IMU.

IV. EXPERIMENT

A. Dataset

We conducted experiments using both public datasets and real-world vehicle tests.

For the public dataset experiments, all sequences are from the MulRan [36] and Boreas [37] datasets. Due to the significant impact of the MulRan in the field of scanning radar

odometry research, we conducted qualitative experiments on it. In contrast, Boreas, which contains a variety of weather conditions but is seldom used, was mainly utilized for qualitative analysis.

The real-world vehicle tests were carried out in a factory area located in the Shunyi District of Beijing. An experimental vehicle, equipped with a scanning radar, an inertial measurement unit (IMU), and real-time kinematic (RTK) positioning, was employed to gather data for these tests. We have designated these data as ‘‘Shunyi’’. The primary aim of the real-world vehicle experiments was to validate the algorithm’s viability for deployment in authentic applications per step.

B. Error Metrics

To verify the performance of the odometry, two indicators are selected: odometry accuracy and runtime. The odometry accuracy was evaluated using the classical method introduced in [38], where we recorded and analyzed the relative translation error (%) and rotation error ($^\circ/100m$) between trajectory segments of varying lengths (e.g., from 100 meters to 800 meters). As for the running time, it is evaluated based on the duration from receiving the radar data to completing the pose estimation.

C. Implementation Details

Noted that the motion distortion compensation in the scanning radar odometry branch of RINO is not always active. Repeated trial results (Fig.6) indicate that constantly enabling dynamic distortion compensation may actually degrade the system’s rotational estimation accuracy. The reason may lie in the low scanning frequency of the scanning radar. Within a scanning cycle (0.25s), the gyroscope in the IMU has already experienced significant drift, and using this to compensate for motion distortion could negatively affect rotation estimation. Considering the gyroscope measurements have relatively less drift when the vehicle undergoes a large rotation, our system imposes thresholds `min_for_mc_` and `max_for_mc_` for the motion distortion compensation module. The module is only activated when the rotation falls between these two threshold values. It has been proven that this strategic motion distortion compensation method indeed enhances the accuracy of the odometry.

Additionally, unlike ORORA, we did not perform voxel-sampling on the pointcloud $\{p_i\}_{i=1}^N$ because we found that this would disrupt the assignment of timestamps to each point.

D. Parameters

The number of parameters in RINO is small which reflects the model’s strong generalization and adaptability to new data. We listed all the parameters in the Tab.I, including those used for testing on the MulRan dataset and those set for real-world tests. The differences between the two sets of parameters are primarily due to the use of a different scanning radar model. It is important to note that the parameters suitable for the MulRan were obtained through adjustments on the DCC01 sequence and were kept fixed during testing on the remaining sequences, as We believe that this approach to renders the experimental results more meaningful.

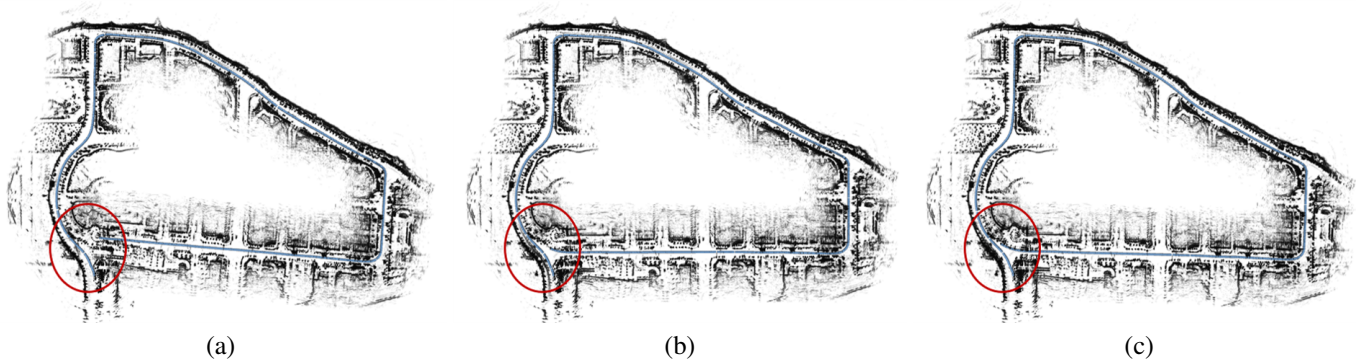


Fig. 6. (a) shows the results obtained with motion distortion compensation enabled at all times; (b) shows the results with motion distortion compensation disabled; (c) displays the outcomes from our strategic motion distortion compensation approach. It can be observed that the overlap of pointcloud structural features at the location indicated by the red circle in (c) is superior compared to that in (a) and (b).

TABLE I
SYSTEM PARAMETER CONFIGURATION

Parameter	Value for MulRan	Value for Shunyi
zw_	3.0	5.0
wf_	17	21
min_for_mc_	2.0°	2.0°
max_for_mc_	9.0°	9.0°
thr_for_stop_	600	400
thr_for_inlier_	0.3	0.1
cbar_radial_	0.1	0.4
cbar_tangential_	0.0262	0.0262

V. QUANTITATIVE EVALUATION

A. Benchmarking

We selected the best odometry or SLAM algorithms using different sensor modalities in large-scale environments as benchmarks. These methods include LOAM [7], SuMa [39], and the state-of-the-art scanning radar odometry algorithms introduced in Sec. II: CFEAR, MC-RANSAC, and ORORA.

We conducted tests on nine sequences from the MulRan dataset: DCC01, DCC02, DCC03, KAIST01, KAIST02, KAIST03, Riverside01, Riverside02, and Riverside03. The detailed results are shown in Tab. II. It is important to note that, due to the unavailability of direct reproductions of these methods, the data in the table is taken from the reported results in publicly published papers. The table categorizes the advanced methods into LiDAR odometry, scan matching-based sparse scanning millimeter-wave radar odometry, and point matching-based sparse scanning millimeter-wave radar odometry. The data in the table is presented in the format (%°/100m), where the former is the relative translation error, and the latter is the relative rotation error.

The proposed exhibits reduced relative translation and rotation errors across the majority of sequences, with particularly impressive performance in the DCC and KAIST datasets. In some sequences, the results outperform the suboptimal algorithm by 21.19%. RINO has significantly improved the performance of the baseline ORORA. Compared to ORORA with Cen2018 and Cen2019 keypoint extraction, RINO has achieved average enhancements of 91.51% and 97.40% in

the DCC and KAIST sequences, respectively. In the DCC03 sequence, the improvement reaches up to 260.4%. Additionally, in contrast to using a LiDAR data source with higher resolution and less motion distortion per frame, RINO has also comprehensively surpassed the classic LiDAR odometry method LOAM, attaining accuracy comparable to the advanced method SuMa.

When RINO runs on the Riverside sequences, there is a significant decline in odometry accuracy compared to the DCC and KAIST sequences. Nonetheless, certain performance metrics remain at the optimal or suboptimal level. On one hand, the data in Riverside sequences were collected along the riverbank, which is considered a degenerate scenario. On the other hand, the performance degradation of RINO is more pronounced compared to other algorithms. A possible reason lies in the assumption of Markovian property inherent in our pipeline. Whether it is the ESKF or the odometry based on global pointcloud registration, both operate in an incremental fashion, where the current pose transformation estimate is only related to the previous time step. This approach, to some extent, overlooks the structural information of point clouds over a larger area in the local map, which can lead to confusion in degenerate environments.

As the aforementioned analysis, we argue that RINO has elevated the optimal accuracy performance of current odometry algorithms designed for adverse weather conditions in structured environments. In terms of test results across all scenarios, RINO is considered to achieve a level of performance that is comparable to the current state-of-the-art algorithms.

B. Ablation Study

Firstly, we replicated the scanning radar odometry method that solves for rotation using gradual non-convex optimization, referred to as RO(GNC), which effectively represents ORORA receiving sensor data through ROS (Robot Operating System). Compared to the code released by ORORA, RO(GNC) employs the keypoint extraction method described in Sec. III-C and does not apply voxel grid filtering to the pointcloud before feature matching. This decision arose from our observations during replication, where we found that performing this step would disrupt the previously assigned timestamps for each keypoint, thereby invalidating the motion distortion

TABLE II
EVALUATION ON 9 SEQUENCES OF THE MULRAN DATASET USING DIFFERENT METHODS AND SENSOR MODALITIES.

Method	Sequence								
	DCC01	DCC02	DCC03	KAIST01	KAIST02	KAIST03	RiverSide01	RiverSide02	RiverSide03
SuMa	2.71/0.4	4.07/0.9	2.14/0.6	2.90/0.8	2.64/0.6	2.17/0.6	1.66/0.6	1.49/0.5	1.65/0.4
LOAM	3.16/0.86	2.64/0.74	2.23/0.74	2.70/0.82	2.80/0.84	7.54/0.79	4.25/0.88	4.14/0.90	4.21/1.02
CFEAR-1	2.44/0.63	1.65/0.54	1.41/0.50	2.12/0.81	1.83/0.74	2.08/0.8	2.30/0.80	2.07/0.66	2.60/0.59
CFEAR-2	2.09/0.55	1.38/0.47	1.26/0.47	1.48/0.65	1.51/0.63	1.59/0.75	1.62/0.62	1.35/0.52	1.19/0.37
MC-RANSAC	4.79/1.27	3.76/1.00	4.39/1.40	-	6.60/1.74	4.67/1.19	4.76/1.08	6.49/1.73	7.72/2.19
MC-RANSAC + DPLR	4.49/1.12	3.64/1.00	4.37/1.39	-	6.32/1.68	4.42/1.12	5.92/1.43	8.38/2.08	6.61/1.88
ORORA(Cen2018)	3.18/0.66	2.38/0.57	2.77/0.79	-	3.12/0.78	2.53/ 0.57	3.51/0.76	3.31/0.76	2.79/0.64
ORORA(Cen2019)	3.12/0.67	2.60/0.51	2.37/0.57	-	3.28/0.82	3.04/ 0.70	3.53/0.84	2.67/ 0.64	2.11/0.49
RINO(Ours)	1.64/0.46	1.25/0.30	0.91/0.39	1.15/0.43	1.42/0.46	2.08/1.08	2.28/0.53	2.35/0.80	2.28/0.47

TABLE III
ABLATION STUDY RESULTS ON 9 SEQUENCES OF THE MULRAN DATASET.

Method	Sequence								
	DCC01	DCC02	DCC03	KAIST01	KAIST02	KAIST03	RiverSide01	RiverSide02	RiverSide03
RO(Graduated Non-Convexity)	4.04/0.92	2.53/0.37	2.26/0.58	3.86/0.77	3.69/0.71	4.86/1.35	4.82/0.75	6.21/1.04	5.18/0.65
RO(Adaptive Voting)	3.52/0.74	3.31/0.52	1.95/0.50	5.11/1.07	4.16/0.70	4.86/1.34	4.23/0.63	5.63/1.08	5.63/0.84
RIO-UC	2.31/0.59	1.46/0.37	1.64/0.46	2.12/0.59	1.70/0.52	2.13/1.10	2.34/0.58	5.07/0.93	3.95/0.60
RIO	2.11/0.55	1.54/0.34	1.55/0.50	1.93/0.54	1.50/ 0.43	2.01/1.03	2.38/0.54	4.97/0.97	4.05/0.54
RIO+MC	1.64/0.46	1.25/0.30	0.91/0.39	1.15/0.43	1.42/0.46	2.08/1.08	2.28/0.53	2.35/0.80	2.28/0.47

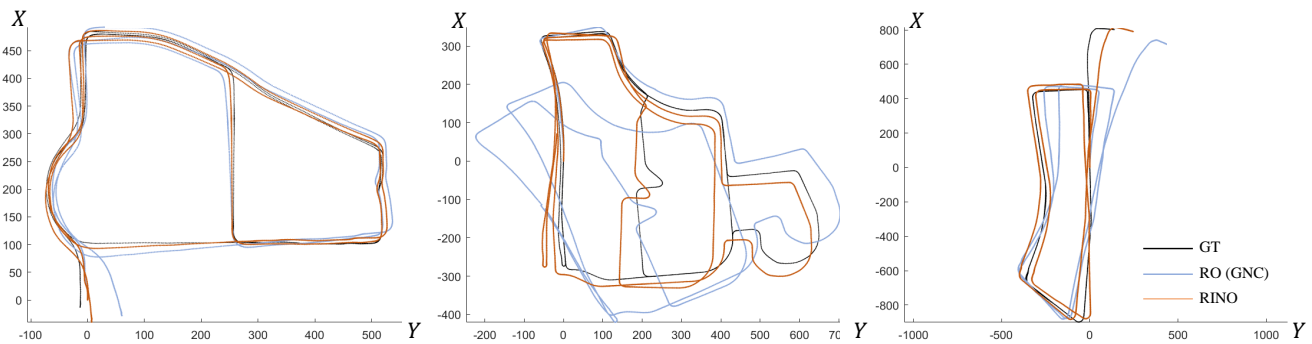


Fig. 7. An intuitive comparison is provided between our method and the baseline method. The black trajectory represents the ground truth, the blue trajectory represents the trajectory estimated by the baseline method, and the orange trajectory represents the trajectory estimated by our method.

compensation process. As a control experiment, we use the scanning radar odometry method that employs adaptive voting to solve for rotation, termed RO(AV), which also represents the scanning radar component of RINO. Subsequently, we compare these two algorithms with the RIO system enhanced with an IMU. In the experiment, we introduce modifications to the RIO system. Specifically, RIO-UC refers to the system where the scanning radar branch no longer outputs uncertainty in the pose estimation, and the noise is fixed at 10^{-2} during all ESKF observations. On the other hand, RIO+MC indicates that RINO incorporates motion aberration compensation with a specific strategy. These variations are used to demonstrate the impact of the uncertainty estimation module and the motion distortion compensation module, as discussed in Sec.IV-C.

The specific test results are detailed in Tab.III. The outcomes indicate that the performance of RO(GNC) is degraded

compared to the test results published in the ORORA paper (Tab.II). We speculate that this degradation may be due to differences in parameter settings and the loss of precise azimuth encoding information in the raw scanning radar data.

When comparing RO(GNC) and RO(AV), the odometry errors of both methods are similar across multiple sequences. However, RO(AV) typically exhibits a shorter runtime than RO(GNC). Moreover, we believe that RO(AV) demonstrates higher robustness compared to RO(GNC). This suggests that using the adaptive voting method for rotation estimation enhances the system's overall performance.

In contrast to these two scanning millimeter-wave radar odometry methods, the integrated localization and mapping system (RIO) achieves a notable improvement across all sequences (74.26%), particularly in sequences DCC01, DCC02, KAIST01, KAIST02, KAIST03, and RiverSide01.

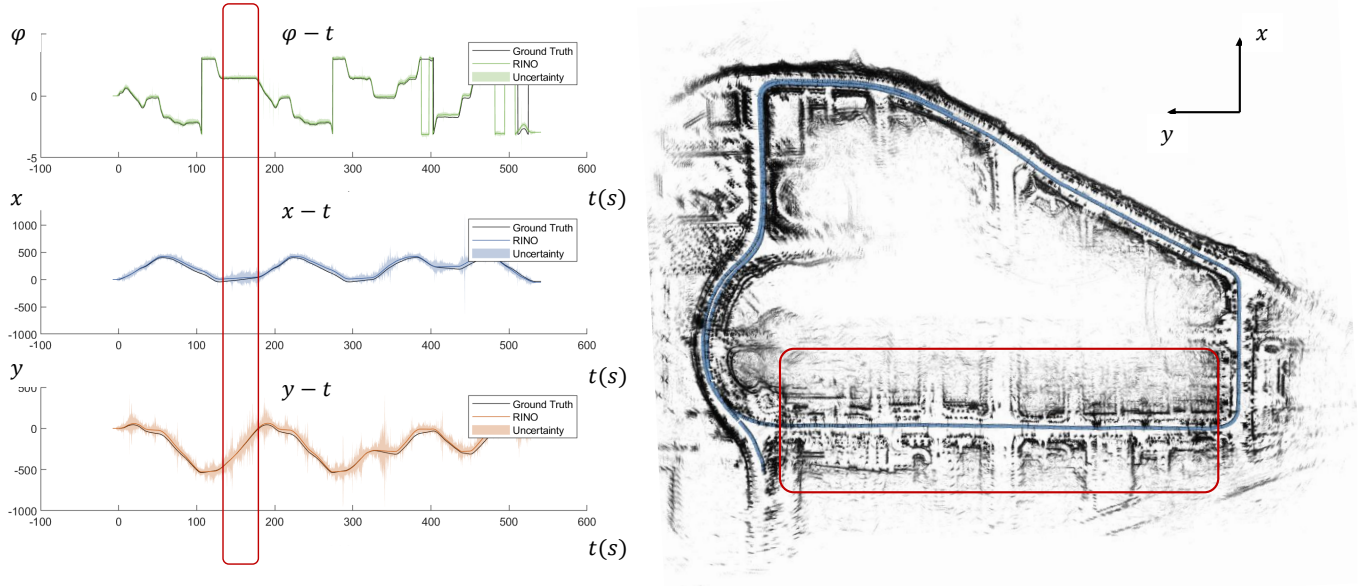


Fig. 8. The pose and uncertainty estimates obtained from the scanning radar odometry on the DCC01 sequence of the MulRan dataset. The uncertainty is represented by scaling the variance of the pose estimate. The red boxes highlight the correspondence between the data in the figure and the vehicle's position in the scene.

This demonstrates that loosely coupling an IMU with the scanning radar odometry significantly enhances the system's accuracy.

If the RINO system does not propagate the uncertainty of the pose estimates, we observe a slight increase in odometry errors in some sequences. This may be attributed to the negative impact of high-uncertainty radar pose estimates on the fusion module. Although the improvement in accuracy from the uncertainty estimation module is not substantial, we believe it provides RINO with the ability to adaptively adjust based on sensor states. This adaptation enables the system to better handle extreme situations, such as sensor failures or scene degradation.

Implementing strategic motion distortion compensation on top of RIO, the experimental results show that motion distortion compensation leads to significant improvements in most sequences (30.59%), except for the KAIST03 sequence. We attribute this phenomenon to the fact that the proposed motion distortion compensation strategy is not an intrinsic solution, but rather an enhancement technique. The unique characteristics of the KAIST03 sequence, which involve more severe vehicle rotations in its trajectory, exceed the scope of the current motion distortion compensation strategy, resulting in a slight decrease in performance.

C. Algorithm Runtime

RINO is capable of real-time operation, as demonstrated in Fig.9. The algorithm's runtime test was conducted using the DCC01 sequence from the MulRan dataset. Our hardware setup includes an Intel® Core i5-13600K processor.

We measured the time each component took to process, from receiving the scanning radar data to completing the

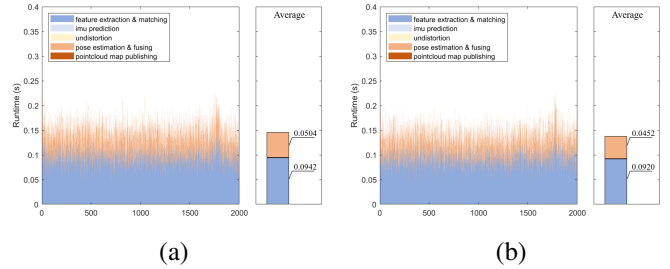


Fig. 9. Runtime comparison of key modules in RO(GNC) (a) and RIO+MC (b) on the DCC01 sequence of the MulRan dataset.

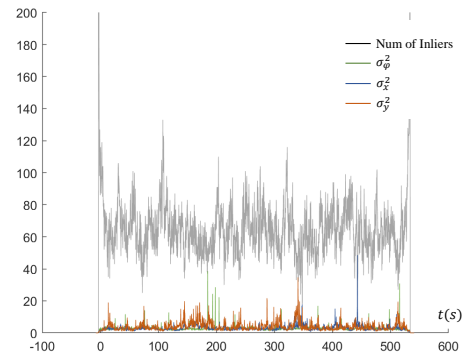


Fig. 10. The relationship between the number of points in the inlier set remaining after Maximum Clique Inlier Selection (MCIS) in point cloud registration and the uncertainty of the pose estimate is shown. As the number of inlier points increases, the uncertainty in the pose estimate generally decreases, reflecting higher confidence in the alignment. Conversely, a smaller inlier set leads to higher uncertainty, indicating less reliable pose estimation.

pose estimation within a single run. Similar to ORORA, the majority of the system's runtime is spent on keypoint extraction and matching. The time consumed by point cloud registration primarily depends on the number of keypoint pairs involved in the coarse matching process. The system's efficiency decreases significantly when the vehicle is moving slowly or stationary.

The average runtime of the system is approximately 0.1381s, which is faster than the scanning millimeter-wave radar data acquisition frequency (4Hz). By comparing Fig.9(a) with Fig.9(b), we observe that the point cloud registration module's efficiency improves by nearly 11.5% due to the adoption of adaptive voting. This enhancement contributes to a more effective solution to the original robust pointcloud registration problem, thus demonstrating the effectiveness of the proposed approach.

D. Pose Estimation Uncertainty

First, we discuss the relationship between the uncertainty of scanning radar pose estimates and the distribution of scene features. The red boxes in Fig.8 indicate regions with higher uncertainty, which correspond to the vehicle traveling along a straight road from right to left. The building features on both sides of the road are distributed along the road, creating a degenerate configuration along the y-axis, which results in higher uncertainty in the y-direction. This observation suggests that pose estimation uncertainty is closely related to the distribution of features in the scene.

Next, we argue that the number of inliers remaining after Maximum Clique Inlier Selection (MCIS) in pointcloud registration also influences the uncertainty of pose estimation. Intuitively, fewer observation sources correspond to lower confidence in the estimate. This is confirmed in Fig.10, where valleys in the number of inliers often align with peaks in pose uncertainty, indicating a direct relationship between the number of inliers and the confidence of the pose estimation.

VI. QUALITATIVE EVALUATION

A. Robustness to severe weather conditions

We present the performance of RINO on the Boreas dataset for the 2021-11-28-09-18 sequence, as shown in Fig.11.

Fig.11 illustrates the synchronized image data captured by the camera. From the camera's perspective, it is evident that the current weather conditions are harsh, with dim lighting, snow-covered ground, and falling snowflakes that partially obscure the camera's view. The weak illumination and the uniformly white snow tend to blur texture features in the camera images, while the floating snowflakes introduce significant noise to the LiDAR scans. These challenging weather conditions have a detrimental effect on visual and LiDAR-based odometry algorithms.

However, the experimental results demonstrate that RINO remains largely unaffected by such adverse weather conditions.

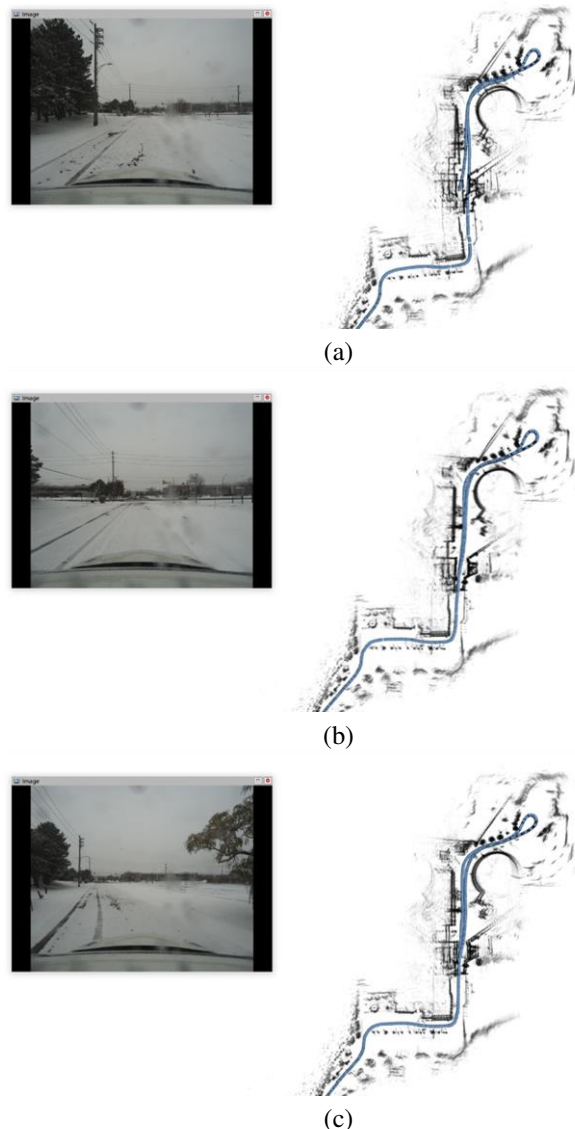


Fig. 11. (a) The complete estimated trajectory (in blue) and the pointcloud map (in black) are shown, obtained using parameters tuned for the MulRan dataset. However, we disabled the IMU prediction and update, meaning that only the results of the scanning radar odometry are displayed. After the vehicle made a U-turn in a confined area, the pointcloud in the revisited region did not align. (b) With the inclusion of the IMU, the odometry performance improved, and the point cloud in the revisited region became clearer. (c) By further enabling the strategically applied dynamic distortion compensation, the point cloud in the revisited region almost completely aligned compared to that in (b).

B. Robustness across diverse scenarios

We validated the feasibility and robustness of RINO by deploying it on real vehicles running in never-before-seen environments.

Our data collection vehicle is a 4x4 off-road platform equipped with a variety of sensors to support different perception tasks, as shown in Fig.12. An Oxts RT3000 high-precision positioning system, which includes an integrated IMU, is installed on the vehicle. A NavTech CIRDEV-X scanning radar is centrally mounted on the roof. The configurations of the other sensors are omitted here for brevity.

The experiment was conducted within a factory in Shunyi



Fig. 12. The sensor system is equipped with a scanning radar and an IMU, which provides the conditions for the fusion of data from both devices.

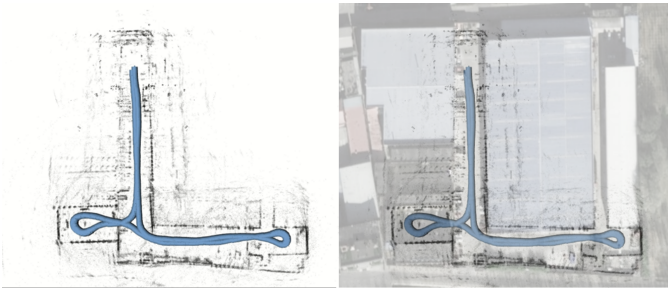


Fig. 13. We present the intuitive trajectory and pointcloud map obtained from the data collected on the 4x4 off-road platform, and it aligns result with the satellite map for comparison.

District, Beijing. The data collection vehicle was driven along two routes. The first route was shorter, intended for parameter tuning (labeled 2024-05-28-17-09), while the second route was longer, forming a closed loop, and used for qualitative evaluation of the fusion localization and mapping system (labeled 2024-05-28-18-48). During the experiment, data from the scanning radar and the IMU were transmitted between the sensors and the industrial computer in ROS message format.

It is noteworthy that the scanning radar used in our setup differs from the models mounted on the vehicles in the MulRan or Boreas datasets, as it has a lower radial resolution (only 0.175m). The original images from the NavTech CIRDEV-X radar exhibit more blurred environmental features and contain significantly more noise. Despite these challenges, the experimental results demonstrate that our algorithm remains robust even with such degraded data, which also highlights the necessity of parameter tuning.

Additionally, the platform is powered by a diesel engine and features a stiff suspension system, leading to significant vehicle body vibrations during traversal. To mitigate IMU measurement errors induced by these vibrations, we implemented a Chebyshev filter. The inclusion of this filtering module has significantly improved the reliability and accuracy of the IMU data.

As shown in Fig.13, the pointcloud map is relatively clear in the revisited regions of both loops. This indicates that, even under complex and aggressive motion conditions, our algorithm maintains high-precision odometry estimation, and the point cloud map accurately reflects the structural features

present on the satellite map.

VII. CONCLUSION

In this work, we have introduced the RINO system, a robust and accurate Radar-Inertial Odometry framework to address the challenge of autonomous navigation for self-driving cars under severe weather conditions. By adopting a non-iterative approach for rotation and translation estimation, RINO significantly improves efficiency while maintaining stable performance. The adaptive voting scheme for 2D rotation estimation and the incorporation of scanning radar pose uncertainty into the Error-State Kalman Filter (ESKF) represent novel contributions that enhance the robustness and accuracy of pose estimation. Our system demonstrates superior performance compared to existing state-of-the-art methods and baselines in both accuracy and resilience.

Key findings include the strategic compensation for motion distortion, the elimination of iterative solving and pose uncertainty estimation, which collectively contribute to the algorithm's success. Additionally, the real-world testing validated the system's performance and robustness, confirming that RINO is well-suited for practical deployment.

From this work, researchers can learn the value of combining radar and IMU data in a non-iterative, loosely coupled framework, and the importance of accurately modeling uncertainty in pose estimation. While RINO outperforms existing methods, it also highlights areas for improvement, such as more effective motion distortion compensation and handling degraded scenarios. Future work will focus on addressing these limitations to further enhance the algorithm's robustness and applicability in real-world autonomous navigation.

REFERENCES

- [1] T. Qin, P. Li, and S. Shen, "Vins-mono: A robust and versatile monocular visual-inertial state estimator," *IEEE Transactions on Robotics*, vol. 34, no. 4, pp. 1004–1020, 2018. [Online]. Available: <https://ieeexplore.ieee.org/document/8421746/>
- [2] C. Campos, R. Elvira, J. J. G. Rodriguez, J. M. M. Montiel, and J. D. Tardos, "Orb-slam3: An accurate open-source library for visual, visual-inertial, and multimap slam," *IEEE Transactions on Robotics*, vol. 37, no. 6, pp. 1874–1890, 2021. [Online]. Available: <https://ieeexplore.ieee.org/document/9440682/>
- [3] W. Guan, P. Chen, Y. Xie, and P. Lu, "PI-evio: Robust monocular event-based visual inertial odometry with point and line features," *IEEE Transactions on Automation Science and Engineering*, vol. 21, no. 4, pp. 6277–6293, 2024.
- [4] H. Jiang, R. Qian, L. Du, J. Pu, and J. Feng, "UI-slam: A universal monocular line-based slam via unifying structural and non-structural constraints," *IEEE Transactions on Automation Science and Engineering*, pp. 1–18, 2024.
- [5] Z. Zhang, Y. Jiao, R. Xiong, and Y. Wang, "Fusing multiple isolated maps to visual inertial odometry online: A consistent filter," *IEEE Transactions on Automation Science and Engineering*, vol. 21, no. 4, pp. 5623–5638, 2024.
- [6] X. Zuo, M. Zhang, M. Wang, Y. Chen, G. Huang, Y. Liu, and M. Li, "Visual-based kinematics and pose estimation for skid-steering robots," *IEEE Transactions on Automation Science and Engineering*, vol. 21, no. 1, pp. 91–105, 2024.
- [7] J. Zhang and S. Singh, "Loam: Lidar odometry and mapping in real-time," in *Robotics: Science and Systems X*. Robotics: Science and Systems Foundation, 2014. [Online]. Available: <http://www.roboticsproceedings.org/rss10/p07.pdf>
- [8] W. Xu and F. Zhang, "Fast-lio: A fast, robust lidar-inertial odometry package by tightly-coupled iterated kalman filter," *IEEE Robotics and Automation Letters*, vol. 6, no. 2, pp. 3317–3324, 2021.

- [9] P. Dellenbach, J.-E. Deschaud, B. Jacquet, and F. Goulette, "Ct-icp: Real-time elastic lidar odometry with loop closure," in *2022 International Conference on Robotics and Automation (ICRA)*, 2022, pp. 5580–5586.
- [10] G. P. C. Júnior, A. M. C. Rezende, V. R. F. Miranda, R. Fernandes, H. Azpúrua, A. A. Neto, G. Pessin, and G. M. Freitas, "Ekf-loam: An adaptive fusion of lidar slam with wheel odometry and inertial data for confined spaces with few geometric features," *IEEE Transactions on Automation Science and Engineering*, vol. 19, no. 3, pp. 1458–1471, 2022.
- [11] C. Xia, X. Li, F. He, S. Li, and Y. Zhou, "Accurate and rapidly-convergent gnss/ins/lidar tightly-coupled integration via invariant ekf based on two-frame group," *IEEE Transactions on Automation Science and Engineering*, pp. 1–14, 2024.
- [12] N. J. Abu-Alrub and N. A. Rawashdeh. Radar odometry for autonomous ground vehicles: A survey of methods and datasets. [Online]. Available: <http://arxiv.org/abs/2307.07861>
- [13] P. J. Besl and N. D. McKay, "A method for registration of 3-d shapes," *IEEE Transactions on Pattern Analysis and Machine Intelligence*, vol. 14, no. 2, pp. 239–256, 1992. [Online]. Available: <https://doi.org/10.1109/34.121791>
- [14] H. Lim, K. Han, G. Shin, G. Kim, S. Hong, and H. Myung. Orora: Outlier-robust radar odometry. arXiv.org. [Online]. Available: <https://arxiv.org/abs/2303.01876v1>
- [15] Y. S. Park, Y.-S. Shin, and A. Kim, "Pharao: Direct radar odometry using phase correlation," in *2020 IEEE International Conference on Robotics and Automation (ICRA)*. IEEE, 2020, pp. 2617–2623. [Online]. Available: <https://ieeexplore.ieee.org/document/9197231/>
- [16] D. Barnes, R. Weston, and I. Posner. (2020) Masking by moving: Learning distraction-free radar odometry from pose information. [Online]. Available: <http://arxiv.org/abs/1909.03752>
- [17] R. Weston, M. Gadd, D. De Martini, P. Newman, and I. Posner. Fast-mbym: Leveraging translational invariance of the fourier transform for efficient and accurate radar odometry. [Online]. Available: <http://arxiv.org/abs/2203.00459>
- [18] D. Adolfsson, M. Magnusson, A. Alhashimi, A. J. Lilienthal, and H. Andreasson, "Cfear radarodometry - conservative filtering for efficient and accurate radar odometry," in *2021 IEEE/RSJ International Conference on Intelligent Robots and Systems (IROS)*, 2021, pp. 5462–5469.
- [19] —, "Lidar-level localization with radar? the cfear approach to accurate, fast, and robust large-scale radar odometry in diverse environments," *IEEE Transactions on Robotics*, pp. 1–20, 2022.
- [20] A. Alhashimi, D. Adolfsson, M. Magnusson, H. Andreasson, and A. J. Lilienthal. Bfar-bounded false alarm rate detector for improved radar odometry estimation. [Online]. Available: <http://arxiv.org/abs/2109.09669>
- [21] P.-C. Kung, C.-C. Wang, and W.-C. Lin, "A normal distribution transform-based radar odometry designed for scanning and automotive radars," in *2021 IEEE International Conference on Robotics and Automation (ICRA)*. IEEE, 2021, pp. 14 417–14 423. [Online]. Available: <https://ieeexplore.ieee.org/document/9561413/>
- [22] R. Zhang, Y. Zhang, D. Fu, and K. Liu, "Scan denoising and normal distribution transform for accurate radar odometry and positioning," *IEEE Robotics and Automation Letters*, vol. 8, no. 3, pp. 1199–1206, 2023.
- [23] Z. Hong, Y. Petillot, and S. Wang, "Radarslam: Radar based large-scale slam in all weathers," in *2020 IEEE/RSJ International Conference on Intelligent Robots and Systems (IROS)*. IEEE, 2020, pp. 5164–5170. [Online]. Available: <https://ieeexplore.ieee.org/document/9341287/>
- [24] Z. Hong, Y. Petillot, A. Wallace, and S. Wang, "Radarslam: A robust simultaneous localization and mapping system for all weather conditions," *The International Journal of Robotics Research*, vol. 41, no. 5, pp. 519–542, 2022. [Online]. Available: <http://journals.sagepub.com/doi/10.1177/02783649221080483>
- [25] D. Barnes and I. Posner, "Under the radar: Learning to predict robust keypoints for odometry estimation and metric localisation in radar," in *2020 IEEE International Conference on Robotics and Automation (ICRA)*, 2020, pp. 9484–9490.
- [26] O. Ronneberger, P. Fischer, and T. Brox, "U-net: Convolutional networks for biomedical image segmentation," in *Medical Image Computing and Computer-Assisted Intervention – MICCAI 2015*, N. Navab, J. Hornegger, W. M. Wells, and A. F. Frangi, Eds. Springer International Publishing, 2015, vol. 9351, pp. 234–241. [Online]. Available: http://link.springer.com/10.1007/978-3-319-24574-4_28
- [27] K. Burnett, A. P. Schoellig, and T. D. Barfoot, "Do we need to compensate for motion distortion and doppler effects in spinning radar navigation?" *IEEE Robotics and Automation Letters*, vol. 6, no. 2, pp. 771–778, 2021.
- [28] H. Yang, J. Shi, and L. Carlone, "Teaser: Fast and certifiable point cloud registration," *IEEE Transactions on Robotics*, vol. 37, no. 2, pp. 314–333, 2021.
- [29] Z. Chen, K. Sun, F. Yang, and W. Tao, "Sc²-pcr: A second order spatial compatibility for efficient and robust point cloud registration," in *2022 IEEE/CVF Conference on Computer Vision and Pattern Recognition (CVPR)*. IEEE, 2022, pp. 13 211–13 221. [Online]. Available: <https://ieeexplore.ieee.org/document/9878510/>
- [30] X. Zhang, J. Yang, S. Zhang, and Y. Zhang, "3d registration with maximal cliques," in *Proceedings of the IEEE/CVF Conference on Computer Vision and Pattern Recognition*, 2023, pp. 17 745–17 754.
- [31] Y. Liang, S. Muller, D. Schwendner, D. Rolle, D. Ganesch, and I. Schaffer, "A scalable framework for robust vehicle state estimation with a fusion of a low-cost imu, the gnss, radar, a camera and lidar," in *2020 IEEE/RSJ International Conference on Intelligent Robots and Systems (IROS)*. IEEE, 2020, pp. 1661–1668. [Online]. Available: <https://ieeexplore.ieee.org/document/9341419/>
- [32] P. R. M. De Araujo, M. Elhabiby, S. Givigi, and A. Noureldin, "A novel method for land vehicle positioning: Invariant kalman filters and deep-learning-based radar speed estimation," *IEEE Transactions on Intelligent Vehicles*, vol. 8, no. 9, pp. 4275–4286, 2023. [Online]. Available: <https://ieeexplore.ieee.org/document/10158411/>
- [33] E. Rublee, V. Rabaud, K. Konolige, and G. Bradski, "Orb: An efficient alternative to sift or surf," in *2011 International Conference on Computer Vision*. IEEE, 2011, pp. 2564–2571. [Online]. Available: <http://ieeexplore.ieee.org/document/6126544/>
- [34] S. H. Cen and P. Newman, "Precise ego-motion estimation with millimeter-wave radar under diverse and challenging conditions," in *2018 IEEE International Conference on Robotics and Automation (ICRA)*, 2018, pp. 6045–6052.
- [35] —, "Radar-only ego-motion estimation in difficult settings via graph matching," in *2019 International Conference on Robotics and Automation (ICRA)*, 2019, pp. 298–304.
- [36] G. Kim, Y. S. Park, and Y. Cho, "Mulran: Multimodal range dataset for urban place recognition," in *Proceedings of the 2020 IEEE International Conference on Robotics and Automation (ICRA)*, 2020, pp. 6246–6253.
- [37] B. Keenan, J. Y. David, and W. Yuchen. Boreas: A multi-season autonomous driving dataset. [Online]. Available: <http://arxiv.org/abs/101689>
- [38] A. Geiger, P. Lenz, and R. Urtasun, "Are we ready for autonomous driving? the kitti vision benchmark suite," in *IEEE Conference on Computer Vision and Pattern Recognition*, 2012, pp. 3354–3361.
- [39] J. Behley and C. Stachniss, "Efficient surfel-based slam using 3d laser range data in urban environments," in *Robotics: Science and Systems XIV*. Robotics: Science and Systems Foundation, 2018. [Online]. Available: <http://www.roboticsproceedings.org/rss14/p16.pdf>

VIII. BIOGRAPHY SECTION



Shuocheng Yang received his B.S. degree in Vehicle Engineering from Xingjian College, Tsinghua University, Beijing, China, in 2024. He is pursuing a Ph.D. degree at the School of Vehicle and Mobility, Tsinghua University. His current research interests include multi sensor fusion localization and SLAM.



Shaobing Xu received his Ph.D. degree in Mechanical Engineering from Tsinghua University, Beijing, China, in 2016. He is currently an assistant professor with the School of Vehicle and Mobility at Tsinghua University, Beijing, China. He was an assistant research scientist and postdoctoral researcher with the Department of Mechanical Engineering and Mcity at the University of Michigan, Ann Arbor. His research focuses on vehicle motion control, decision making, and path planning for autonomous vehicles. He was a recipient of NSFC excellent young scholars fund, the outstanding Ph.D. dissertation award of Tsinghua University and the best paper award of AVEC'2018 and AVEC'2020.



Yueming Cao is currently an undergraduate student majoring in Vehicle Engineering at Xingjian College, Tsinghua University, Beijing, China. He is expected to graduate in June 2025 and move on to a Ph.D. degree at the School of Vehicle and Mobility, Tsinghua University. His current research interests include multi sensor fusion localization and decision-making of autonomous vehicles



Shengbo Li (Senior Member, IEEE) received the M.S. and Ph.D. degrees in vehicle engineering from Tsinghua University, Beijing, China, in 2006 and 2009, respectively. He was with Stanford University, Stanford, CA, USA, University of Michigan, Ann Arbor, MI, USA, and the University of California, Berkeley, Berkeley, CA, USA. He is currently a tenured Professor with Tsinghua University. His active research interests include intelligent vehicles and driver assistance, reinforcement learning and distributed control, optimal control and estimation, etc. He is the author of more than 100 journal/conference papers, and the coinventor of more than 20 Chinese patents.



Jianqiang Wang received the B. Tech. and M.S. degrees from Jilin University of Technology, Changchun, China, in 1994 and 1997, respectively, and the Ph.D. degree from Jilin University, Changchun, in 2002. He is currently a Professor and the Dean of the School of Vehicle and Mobility, Tsinghua University, Beijing, China. He has authored over 150 papers and is a co-inventor of over 140 patent applications. He was involved in over 10 sponsored projects. His active research interests include intelligent vehicles, driving assistance systems, and driver behavior. He was a recipient of the Best Paper Award in the 2014 IEEE Intelligent Vehicle Symposium, the Best Paper Award in the 14th ITS Asia Pacific Forum, the Best Paper Award in the 2017 IEEE Intelligent Vehicle Symposium, the Changjiang Scholar Program Professor in 2017, the Distinguished Young Scientists of NSF China in 2016, and the New Century Excellent Talents in 2008.